A FIELD EMISSION AND SECONDARY EMISSION MODEL IN OPAL

C. Wang*, A. Adelmann, Y. Ineichen, PSI, Villigen, Switzerland

Abstract

Dark current and multipacting phenomena, as observed in accelerator structures, are usually harmful to the equipment and the beam quality. These effects need to be suppressed to guarantee stable operation. Large scale simulations can be used to understand the cause and develop solutions for these phenomena. We extend OPAL [1], a parallel framework for charged particle optics in accelerator structures and beam lines, with the necessary physics models to simulate multipacting phenomena. This is achieved by adding a Fowler-Nordheim field emission model and a secondary emission model, as well as 3D boundary geometry handling capabilities to OPAL. With these capabilities we can evaluate dark current and multipacting in high-gradient linac structures and in RF cavities of high intensity Cyclotrons. In state of the art accelerator structures the electric fields are strong, therefor space charge effects in the Fowler-Nordheim model cannot be neglect. In a first step we add the Child-Langmuir model to phenomenologically model space a charge limited field emission. In the near future a multigrid preconditioned iterative space charge solver capable of handling complicated boundary geometries will be used to make our field emission model more self-consistent.

INTRODUCTION

Dark current and multipacting phenomena have been observed in various RF structures of accelerators, e.g. [2] [3]. These phenomena are usually harmful to the equipment and beam quality, as they will cause galvanic etching on the surface of the cavity and thus cause RF breakdown. In this paper we will discuss our efforts to extend OPAL in order to get a feasible tool for performing large scale dark current and multipacting simulations. This would allow more thorough analysis and a deeper understanding of these phenomena. Accurate simulations could lead to methods how these situations can be prevented or diminished. To achieve these goals, first we introduce a particle-boundary collision test model into OPAL to facilitate the particle searching during tracking process. In a subsequent step we add surface physics models including an analytic Fowler-Nordheim field emission model and a phenomenological secondary emission model to OPAL.

The Child-Langmuir space charge model for emitted electrons is discussed here. A multigrid preconditioned iterative space charge solver able to treat complicated boundaries with higher accuracy is still work in progress and will be incorporated in the near future.

* C.Wang is on leave from China Institute of Atomic Energy.

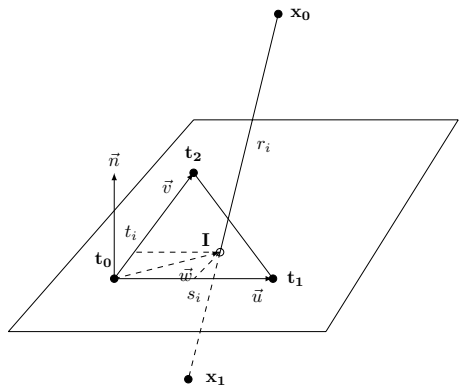

Figure 1: Line segment-triangle intersection.

A code benchmark of the implemented secondary emission model and visualization results are given in the last section of the paper.

PARTICLE-BOUNDARY COLLISION TEST MODEL IN OPAL

Testing particle-boundary collisions is crucial to both dark current and multipacting simulations. We need an efficient way to distinguish between dark current particles potentially reaching the beam diagnostic equipment (e.g. a screen) and those hitting the surface of beam line elements causing multiplication.

The particle-boundary collision test in a 3D geometry is complicated and computational expensive. Our complex 3D geometries are hard to parameterized by simple functions. Instead we represent geometries as triangulated surface meshes. Subsequently we can make use of efficient 3D line segment-triangle intersection (LSTI) tests to find particle-boundary collisions. In the following we will describe how we implemented this collision tests while still retaining code efficiency.

The Line Segment-Triangle Intersection (LSTI) Test

An efficient LSTI test algorithm is described in [4]. Since we need to precompute all triangle normals for triangle orientation anyway we can make use of a faster algorithm relaying on having triangle normals available [5]. In order to compute a LSTI we need the starting and end point of the line segment under consideration, triangle vertices and normal. A schematic view is sketched in Figure 1. Vectors are denoted with arrows (i.e. $\vec{n}$), points (here in $\mathcal{R}^3$) are bold (i.e. $\mathbf{x}_0$) and the remaining symbols de-

note scalars. The algorithm for handling LSTI is given in Algorithm 1.

Algorithm 1 LSTI

procedure LSTI(**In:** $\mathbf{x}_0$, $\mathbf{x}_1$, $\Delta(\mathbf{t}_0, \mathbf{t}_1, \mathbf{t}_2)$, **Out:** isInside, **I**)
if $\vec{n} \cdot (\mathbf{x}_1 - \mathbf{x}_0) = 0$ **then**
  return false {$\mathbf{x}_1 - \mathbf{x}_0$ || $\Delta \rightarrow$ no intersection}
else
  $r_i \leftarrow \frac{\vec{n}\cdot(\mathbf{t}_0-\mathbf{x}_0)}{\vec{n}\cdot(\mathbf{x}_1-\mathbf{x}_0)}$
  $\mathbf{I} \leftarrow \mathbf{x}_0 + r_i(\mathbf{x}_1 - \mathbf{x}_0)$ {The intersection point of the line segment and planed}
  if $r_i < 0$ **or** $r_i > 1$ **then**
    return false {early rejection: intersection is on the extension of line segment}
  else
    {Check if the intersection point is inside the triangle}
    Solve: $\vec{w} = \mathbf{t}_0 + s_i\vec{u} + t_i\vec{v}$ {parametric plane equation}
    $s_i \leftarrow \frac{(\vec{u}\cdot\vec{v})(\vec{w}\cdot\vec{v})-(\vec{v}\cdot\vec{v})(\vec{w}\cdot\vec{u})}{(\vec{u}\cdot\vec{v})^2-(\vec{u}\cdot\vec{u})(\vec{v}\cdot\vec{v})}$
    $t_i \leftarrow \frac{(\vec{u}\cdot\vec{v})(\vec{w}\cdot\vec{u})-(\vec{u}\cdot\vec{u})(\vec{w}\cdot\vec{v})}{(\vec{u}\cdot\vec{v})^2-(\vec{u}\cdot\vec{u})(\vec{v}\cdot\vec{v})}$
    if $s_i \geq 0$ **and** $t_i \geq 0$ **and** $s_i + t_i \leq 1$ **then**
      return (true, **I**)
    else
      return false {no intersection between line segment and triangle}
    end if
  end if
end if
end procedure

Early Rejection Strategy

Even though the implemented LSTI algorithm using precomputed triangle normal is fast a huge number of LSTI calls are necessary. If we have M triangles and N particles in the simulation, both in the magnitude of hundreds of thousand to millions, the number of LSTI tests in single time step without a early rejection strategy would be $M \times N$, i.e., at least 10^{10} per time step. Obviously, effective early rejection strategies (see Figure 2) are needed to reduce the number of LSTI tests.

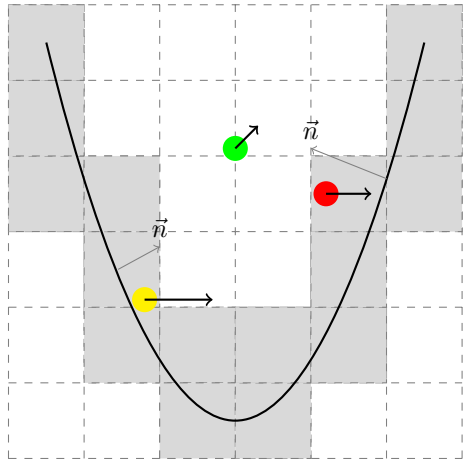

Figure 2: Schematic view of particle-boundary early rejection strategy. The dark black line represents the boundary surface, particles are colored dots with an attached momenta arrow and inward normals gray arrows.

Assuming we need to determine whether a particle with position $\mathbf{r}$ and momenta $\mathbf{p}$ hits the boundary within time step Δt we apply the following early rejection strategies:

- Test if the particle is near the boundary by checking if $\mathbf{r}$ is inside the boundary bounding boxes (illustrated by gray grids in Figure 2).
- If $\mathbf{r}$ is not in a bounding box (green particle in Figure 2), the particle is enough far away from boundary and can be integrated directly.
- If $\mathbf{r}$ is in a bounding box (yellow particle and red particle in Figure 2), then we check all triangles in the bounding box (of the corresponding particle) as well as triangles in the adjacent 26 bounding boxes to see if the momenta of the particle has a opposite direction with those triangles' normals.
- If the momenta and triangle normal are not opposite for all triangles checked (the yellow particle) do particle integration.
- If they are opposite (red particle) check if the particle has an intersection with the triangles by performing the LSTI test for each triangle. If an intersection exists the particle will hit the boundary during the current time step.

Two things need to be pointed out. First we get the inward normal in the following way. We find a point close to a triangle with specified ID (e.g. 0) and determine if the point is inside or outside the boundary geometry. This can be achieved by doing a ray-boundary intersection test and counting the number of intersections. Using this point we can get the orientation (inward normal) of the triangle with ID 0. Now we can get the inward normal of all surface triangles by recursively aligning the orientation of adjacent

triangles of triangles whose inward normals have already been computed.

Secondly the success of the above particle-boundary collision test relies on the fact that the distance a particles travel in one time step cannot be larger than the bounding box size. Choosing an appropriated bounding box size ensures that a particle will never jump over a bounding box in one time step.

SURFACE PHYSICS MODELS

Field Emission Model

Field emission is a major source of both dark current particles and primary incident particles in secondary emission. The Fowler-Nordheim (F-N) formula we use here to predict the emitted current density is given in (1) [6] [7]

$$J(\mathbf{r},t) = \frac{A(\beta E)^2}{\varphi t(y)^2} \exp\left(\frac{-Bv(y)\varphi^{3/2}}{\beta E}\right) \left[\mathrm{A}/m^2\right] \quad (1)$$

where $J(\mathbf{r},t)$ stands for emitted electric current density in position $\mathbf{r}$ and time t. The Greek letters φ and β denote the work function of the surface material and the local field enhancement factor respectively. The parameter E is the electric field in the normal direction of surface. The parameters A and B are empirical constants. The functions $v(y)$ and $t(y)$ representing the image charge effects [6] as a function of the Fowler-Nordheim parameter y with the following definition [2]

$$y = \sqrt{\frac{e^3}{4\pi\varepsilon}} \frac{\sqrt{\beta E}}{\varphi} = 3.795 \times 10^{-5} \frac{\sqrt{\beta E}}{\varphi}. \quad (2)$$

In our model, we have choosen a simpler approximation originated by J. H. Han [2]

$$\begin{aligned} v(y) &= a - by^2 \\ t(y) &\approx 1. \end{aligned}$$

These approximations are valid for a large range of y, corresponding to typical applied electric field ranges in RF guns.

Users can customize dark current simulation by specifying the value of the work function φ, local field enhancement factor β and other parameters present in (1) and (2) in the OPAL input file.

Space Charge Limited Current Density

Whenever the normal components of an electric field are strong enough the field emission current density will be limited by space charge effect [6]. To cover this situation we incorporated the 1D Child-Langmuir law

$$\begin{aligned} J(\mathbf{r},t) &= \frac{4\varepsilon_0}{9}\sqrt{2\frac{e}{m}}\left(\frac{V^{3/2}}{d^2}\right) \\ &= \frac{4\varepsilon_0}{9}\sqrt{2\frac{e}{m}}\left(\frac{E^{3/2}}{d^{1/2}}\right) \left[\mathrm{A}/m^2\right] \end{aligned} \quad (3)$$

into our field emission model. $J(\mathbf{r},t)$ denotes space charge limited emission current density in position $\mathbf{r}$ and time t, ε_0 the permittivity in vacuum, E the normal component of electric field on the surface and d the distance from the position where E is evaluated. Currently we choose d to be equal to the distance travelled by emitted particles in one time step, i.e., $d = \frac{eE\Delta t^2}{2m_0}$ where Δt is simulation time step.

A multigrid preconditioned iterative space charge solver developed by Adelmann et al. [8] has already been implemented in OPAL. We are in the process of adapting the solver to be able to cope with the geometric boundaries present in our simulations.

Secondary Emission Model

Our implementation of the secondary emission model is based on a phenomenological model developed by M. A. Furman and M. Pivi [9]. This choice was based on the self-consistency property this particular secondary model offers. In this context self-consistency means that if we define one incident electron and the followed secondary emission procedure as an event, the event generator is constructed so that

1. when averaging over an infinite number of secondary-emission events, the reconstructed secondary emission yield δ and its energy spectrum $d\delta/dE$ are guaranteed to agree with the corresponding input quantities
2. the energy integral of $d\delta/dE$ is guaranteed to equal δ
3. the energy of any given emitted electron is guaranteed not to exceed the primary energy
4. the aggregated energy of the electrons emitted in any multi-electron event is also guaranteed not to exceed the primary energy.

This model calculates the number of secondary electrons that result from an incident electron of a given energy on a material at a given angle (see Figure 3). For each of the generated secondary electrons the associated process: *true secondary*, *rediffused* or *backscattered* is recorded.

The basic computational procedure of the secondary emission model is shown in Figure 4.

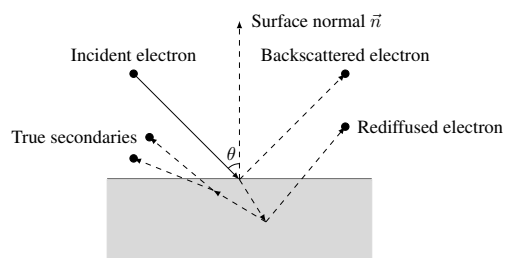

Figure 3: Geometry used by the secondary electrons model.

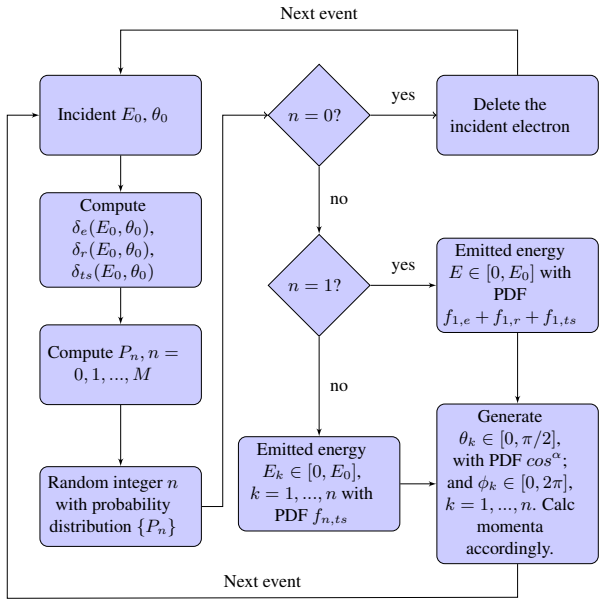

Figure 4: Basic computational procedure of secondary emission model.

CODE BENCHMARK AND RESULT VISUALIZATION

Code Benchmark on Secondary Emission Model

In order to validate the secondary model implemented in OPAL, we conducted a code to code comparison with the TxPhysics library [10]. The simulation parameters were fixed to a large number of incident events (10000) with the same energy (300eV) and the same incident angle (normal to the surface). Figure 5 shows the result of the comparison between OPAL and TxPhysics. We note that the statistical agreement is very good.

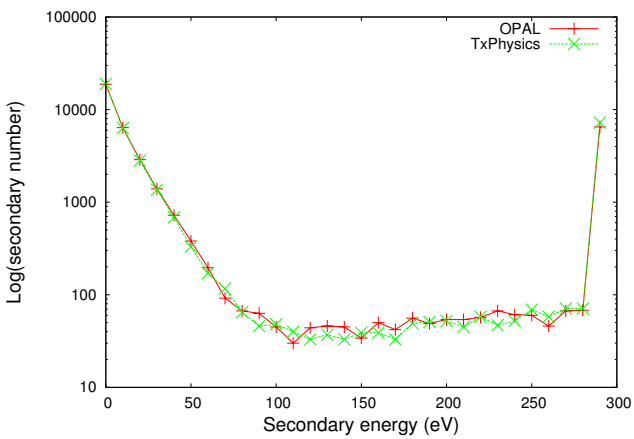

Figure 5: Secondary energy comparison between OPAL and TxPhysics.

Result Visualization

For visualization purposes the boundary geometry is stored into a VTK legacy file. Phase space data of all particles is dumped into a H5Part [11]. With a separate post processing code the H5Part particle data is converted to a VTK legacy file At this point the VTK files can be visualized by tools like . Paraview [12] . A sample visualization of a dark current simulation result is shown in Figure 6.

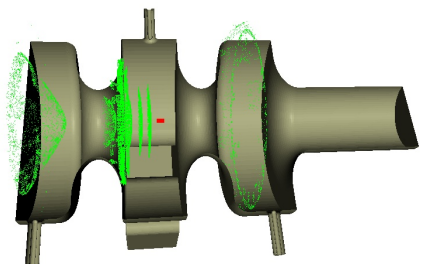

Figure 6: Simulation visualization. Dark current (green) and bunch (red) particles inside PSI XFEL gun.

REFERENCES

[1] A. Adelmann and Ch. Kraus and Y. Ineichen and J. Yang, The OPAL (Object Oriented Parallel Accelerator Library) Framework, Paul Scherrer Institute, PSI-PR-08-02, 2008

[2] J. H. Han, PhD Thesis, Desy, 2005 Available Online on `http://www-library.desy.de/preparch/desy/thesis/desy-thesis-05-045.pdf`

[3] P. K. Sigg, Reliability of High Beam Power Cyclotron RF-Systems at PSI, Proceedings of the Workshop on Utilization and Reliability of High Power Proton Accelerators: Aix-en-Provence, France, 22-24 November 1999. Available Online on: `http://rf.web.psi.ch/files/proceedings/1998/JAERI98/PaperNEA98.pdf`.

[4] T. Möller and B. Trumbore, ACM SIGGRAPH 2005 Courses, July 31-August 04, 2005, Los Angeles, California [doi:10.1145/1198555.1198746]

[5] D. Sunday, Available Online on: `http://softsurfer.com/Archive/algorithm_0105/algorithm_0105.htm`

[6] Y. Feng and J. P. Verboncoeur, Phys.Plasmas 13, 073105 (2006)

[7] R. H. Fowler and L. Nordheim, Proc. R. Soc. London, Ser. A 119, 173 (1928)

[8] A. Adelmann, P. Arbenz and Y. Ineichen, J. Comp. Phys, 229 (12): 4554-4566 (2010)

[9] M. A. Furman and M. T. F. Pivi, Phys. Rev. ST Accel. Beams 5, 124404 (2002)

[10] TxPhysics Users Manual, `http://txphysics.txcorp.com`

[11] A. Adelmann, R.D. Ryne, J. Shalf, C. Siegerist, Particle Accelerator Conference (PAC05), Knoxville TN., May 16-20, 2005.

[12] A. Henderson, ParaView Guide, A Parallel Visualization Application. Kitware Inc., 2007. `http://www.kitware.com/products/paraview.html`